
WarpHammer: Densifying Scene Warps with 3D Object Priors for Extreme View Synthesis

Michael Green¹, Gavriel Habib¹, Dvir Samuel², Tal Berkovitz Shalev¹
Issar Tzachor¹, Rami Ben-Ari^{1,*}, Or Litany^{3,2,*}

¹OriginAI, Israel ²NVIDIA ³Technion

* Authors jointly supervised this work.

Project page: pihash2k.github.io/extreme_nvs

Abstract

Projection-conditioned novel view synthesis (NVS) warps an explicit 3D reconstruction of the input view into the target camera and conditions a generator on the warped rendering. This works well for small viewpoint changes but degrades sharply under large orbital motion: the warp becomes sparse around the orbited object, where hidden surfaces dominate the new view and mirror-like artifacts emerge, causing the generator to lose both pixel content and the implicit camera cue carried by the warp. We introduce WarpHammer, a training-free framework that resolves this failure mode by augmenting the warped scene with an explicit 3D reconstruction of the object obtained from a native 3D generative prior (e.g., SAM3D). The reconstructed object adds missing foreground surfaces and occludes background points that should no longer be visible, restoring both appearance and camera cues without fine-tuning the base model. The same explicit object representation further unlocks a capability current NVS pipelines do not support: incorporating auxiliary views of the object from sources outside the target scene, for example, a casual snapshot of a car paired with a manufacturer studio shot of the same model. We process the reference and auxiliary images jointly with a pretrained multi-view geometry foundation model, which predicts a unified point cloud that we fuse into the 3D object reconstruction. This yields substantially more faithful geometry than single-image reconstruction, without requiring user-provided camera poses for the auxiliary views. On five benchmarks, WarpHammer produces stable novel views at viewpoint deviations where strong baselines collapse, and is the first scene-level NVS method that can naturally fuse auxiliary, pose-unknown object views from an external source.

1 Introduction

Novel view synthesis (NVS) from a single image or a sparse set of views is fundamentally underconstrained: the input does not contain sufficient evidence to recover unobserved regions of the scene. Recent works have therefore shifted from purely per-scene reconstruction to learned visual priors. These include pretrained image generators [36, 40], multi-view generative models [28, 30, 31, 60], and video generators [6, 10, 26]. Trained on large-scale visual data, these models learn statistical regularities that enable plausible completion of missing scene content.

A central design question is how to condition such generators on the desired target viewpoint. Two paradigms are common. Camera-conditioned methods encode the target camera directly, for example through Plücker ray maps or pose embeddings, and rely on the generative model to infer the scene structure end-to-end [16, 21, 23, 47, 60]. Projection-conditioned methods instead lift

the input image into an explicit 3D proxy, typically a point cloud obtained from monocular depth, render this proxy from the target camera, and condition the generator on the resulting warped image [7, 12, 19, 29, 33, 39, 52, 54, 55, 57]. By explicitly tying the conditioning signal to the target camera, projection-conditioned methods provide strong camera control and have achieved state-of-the-art performance on several NVS benchmarks [19, 39]. We build on this paradigm.

However, both paradigms remain brittle under large viewpoint extrapolation. Camera-conditioned models can generalize poorly when the requested camera motion falls outside the training distribution, leading to drift in geometry and pose consistency [49]. Projection-conditioned methods fail for a different and more explicit reason: as the target viewpoint moves away from the input, the warped point cloud — which only contains surfaces visible in the source — leaves growing holes in the conditioning signal, with mirror-like duplicated surfaces emerging around foreground objects [58]. This is particularly damaging because the warp plays two roles: it provides pixel-level appearance evidence, and it implicitly encodes the target camera. When it goes sparse, the generator loses both, and baseline methods exhibit rapidly increasing pose and reconstruction errors under large orbital motion (Fig. 1).

We introduce WarpHammer, a training-free framework that mitigates this failure mode by densifying the warped conditioning signal with an explicit object-centric 3D prior. Our key observation is that the scene warp is most unreliable exactly where object geometry matters most: on the newly visible surfaces of the central object. We augment the standard scene cache with a reconstructed 3D object from a native 3D generative model. The reconstructed mesh plays a dual role: it adds geometry for newly visible object surfaces, and it occludes background points that should no longer be visible once the camera has orbited past the object, thus eliminating the background leakage that scene-only warps suffer from at large angles.

A key aspect of our design is the separation between geometry and appearance. Native 3D generators (e.g., Hunyuan3D, TRELIS) provide reliable shape but their texture and illumination may deviate from the reference scene. We therefore use the reconstruction as geometric guidance only, leaving the diffusion model’s scene-identity conditioning responsible for appearance.

Beyond improving single-image extreme-view synthesis, the explicit object representation enables a second capability that standard warp-based pipelines do not naturally support: incorporating an auxiliary object view from outside the target scene. For example, a dashcam image may contain a car from one viewpoint, while a catalog or manufacturer image may show the same or a related car from another viewpoint. These auxiliary images are typically unposed, and visually mismatched with the reference scene. We address this setting by using a pretrained multi-view geometry foundation model, to jointly process the reference and auxiliary object views. The model predicts object pointmaps in a shared coordinate frame, allowing the auxiliary geometry to be aligned and fused into the reference object reconstruction without requiring camera calibration from the user. To avoid transferring inconsistent color or texture from the auxiliary image, its rendered contribution is injected as an appearance-neutral conditioning signal. Thus, the auxiliary view provides structural evidence for missing object surfaces while the generated video remains anchored to the appearance and context of the reference scene.

Together, these design choices yield a training-free framework that handles extreme-view NVS from a single image and naturally extends to auxiliary-view inputs. Our contributions are:

- We introduce a training-free augmentation to projection-conditioned scene NVS that addresses large-angle view synthesis by densifying sparse target-view warps with an explicit object-centric 3D reconstruction.
- We define and address an auxiliary-view NVS setting, where an unposed object image from an external source is fused into the reference scene as structural evidence rather than as a calibrated scene view.
- We propose an appearance-aware fusion strategy that separates object geometry from appearance, enabling auxiliary views to improve structure without forcing inconsistent color, texture, or illumination into the output.
- We introduce a benchmark for unposed object-view fusion and evaluate across single-view and auxiliary-view regimes on five datasets.
- We introduce OrbErr, an orbital-fidelity metric for object-centric NVS that jointly measures viewpoint correctness and spatial consistency of object features.

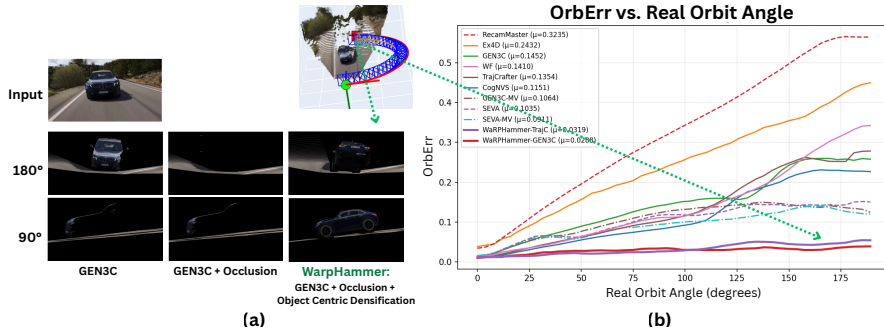


Figure 1: Object-centric densification improves extreme-view synthesis. **(a) Qualitative:** GEN3C shows sparsity and artifacts; WarpHammer remains geometry-consistent. **(b) Quantitative:** OrbErr vs. angle: baselines degrade beyond $\sim 110^\circ$, while WarpHammer maintains low error.

2 Related Work

Sparse-view and multi-view NVS. Classical NVS methods such as NeRFs [5, 34] and 3D Gaussian Splating [24] achieve high-quality rendering from dense posed views, while generalizable methods reduce the number of inputs using learned priors [45, 53, 61]. However, these methods still assume views from the same calibrated scene. WarpHammer instead allows an auxiliary object image to be unposed, out-of-scene, and appearance-mismatched, treating it as structural evidence rather than as another calibrated scene view.

Object-centric generative view synthesis. A parallel line of work uses generative priors for single-image object view synthesis. Zero-1-to-3 learns camera-conditioned novel-view generation from a single object image [28]. SyncDreamer and Wonder3D improve multi-view consistency by jointly generating synchronized views, normals, or other geometry-aware intermediates [30, 31]. SV3D extends this idea with video diffusion and explicit orbital camera control [43], while SV4D produces multi-frame, multi-view consistent videos for dynamic objects [51]. Zero-to-Hero further improves single-image NVS at challenging viewpoints through training-free attention-map manipulation at inference [41]. These methods demonstrate that generative models encode strong object-level 3D priors, but they typically synthesize isolated objects on clean backgrounds and stop short of integrating objects back into a real reference scene with its original lighting and surroundings. WarpHammer instead uses object-centric 3D generation as structural guidance inside a scene-level NVS pipeline. The reconstructed object geometry is fused into the reference scene cache, while appearance, lighting, and background context remain anchored to the reference image.

Camera-controlled and projection-conditioned generative NVS. Recent video diffusion models enable camera-controllable generation from images or monocular videos by injecting camera motion through learned pose embeddings, Plücker rays, relative position encodings, or dedicated control branches [2, 3, 17, 18, 25, 32, 46]. These approaches provide flexible camera control, but the camera signal is mostly implicit, and object geometry may drift under large viewpoint changes.

Projection-conditioned methods make the camera conditioning more explicit. They lift the source image or video into a 3D proxy, render it from the target camera, and use the resulting warp to guide a diffusion model. ViewCrafter [55] and TrajectoryCrafter [54] follow this strategy for single-image and monocular-video inputs, respectively, while GEN3C [39] maintains a persistent 3D cache for world-consistent generation. SEVA [60] accepts posed input views and target cameras, and related methods explore learned camera encoders or inference-time motion guidance [42, 56]. However, these methods ultimately condition on geometry visible in the input view. As the target camera moves to large angles, hidden object surfaces must be hallucinated by the diffusion prior. WarpHammer addresses this limitation by augmenting the scene warp with an explicit object-centric 3D reconstruction, optionally strengthened by an auxiliary object view.

Geometry-completed proxies for large-viewpoint synthesis. Several recent methods also improve large-viewpoint synthesis by constructing more complete geometric proxies. CogNVS reconstructs

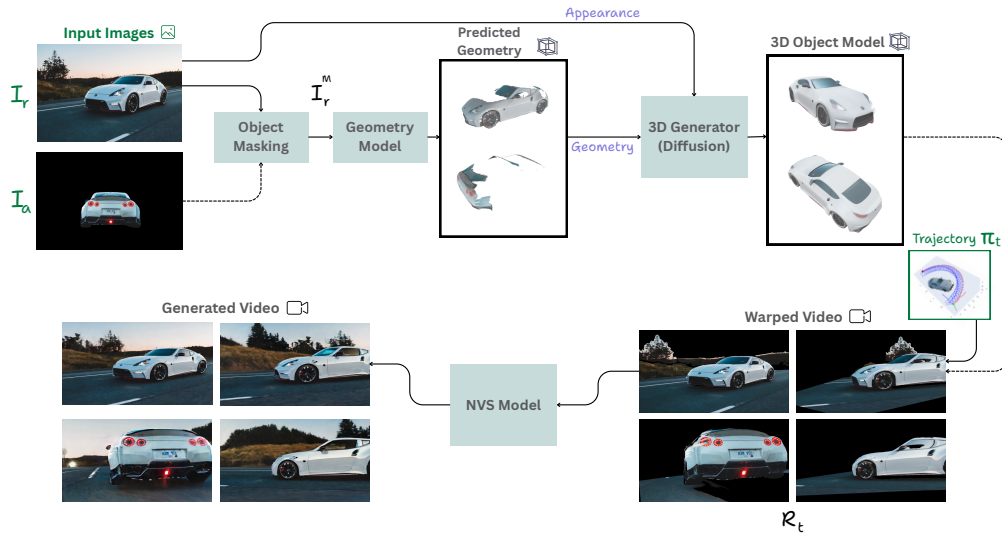


Figure 2: **Overview of WarpHammer.** From a reference image I_r and target trajectory $\{\pi_t\}_{t=1}^T$ (and an optional auxiliary object image I_a), WarpHammer builds a densified point-cloud cache by augmenting the scene warp with an explicit 3D object reconstruction, optionally fused with I_a via a multi-view geometry foundation model, and renders it to condition a video diffusion prior.

co-visible regions from monocular video, inpaints hidden regions, and applies test-time finetuning for temporal coherence [11]. EX-4D uses a depth-watertight mesh as guidance for extreme-viewpoint 4D synthesis [19]. Concurrent work FreeOrbit4D [8] builds on VACE [22] depth conditioning to complete foreground and background geometry for arbitrary camera redirection in monocular videos. These methods are closely related in spirit, since they also use completed geometry as a guide for diffusion-based synthesis. The main distinction is the source and use of the geometry. Prior work primarily derives the proxy from monocular video or depth and targets dynamic or 4D content. WarpHammer targets single-image static-scene NVS, using a native 3D generative prior for object geometry and optionally refining it with an unposed external object image.

3 Method

WarpHammer is a training-free framework for projection-conditioned novel view synthesis whose central operation is the *densification* of the warped scene cache: where a single-image warp goes sparse around a central object at large viewpoint changes, we inject an explicit 3D reconstruction of that object so the conditioning signal handed to the video diffusion prior is dense, geometrically faithful, and camera-aligned. We first describe the single-image pipeline (§3.1–§3.2), then show how the same machinery extends to an auxiliary, unposed object view from a different scene (§3.3).

Problem setup. We assume the reference scene image $I_r \in \mathbb{R}^{H \times W \times 3}$ contains a dominant foreground object — the *central object* — around which the target camera trajectory orbits. Given I_r and a trajectory $\{\pi_t\}_{t=1}^T$ specified *relative* to the input view, our goal is to synthesize a novel-view video $V_g \in \mathbb{R}^{T \times H \times W \times 3}$ that follows the trajectory while preserving scene appearance and object identity. §3.3 extends this setup with an additional, uncalibrated auxiliary image I_a of the same object, possibly captured in a different scene and under different illumination.

3.1 Preliminaries: Projection-Conditioned NVS via Scene Caches

We build WarpHammer on top of two representative backbones: GEN3C [39] and TrajectoryCrafter [54], both of which lift the reference image into a point cloud via monocular depth estimation, render it along the target trajectory, and condition a video diffusion prior on the resulting

warped buffers. We describe the lifted geometry abstractly as a *cache*

$$\mathcal{C} = \{P, A\}, \quad P \subset \mathbb{R}^3, \quad A \in \mathbb{R}^{|P| \times 3}, \quad (1)$$

where P are the lifted scene points and A their RGB attributes; trajectory poses $\{\pi_t\}$ are expressed relative to the reference camera. Rendering \mathcal{C} along $\{\pi_t\}_{t=1}^T$ produces warped renderings $\{R_t\}_{t=1}^T$ and validity masks $\{M_t\}_{t=1}^T$ that anchor synthesized frames to the input scene while leaving the diffusion prior to fill newly visible regions.

3.2 Densifying the Object with a 3D Object Prior

The object is where sparsity hurts most, and where it matters most: background regions typically remain supported as the camera translates, but the object’s hidden surfaces become dominant the moment the camera orbits — precisely the surfaces that define its identity. We address this directly by densifying the foreground cache with an explicit 3D reconstruction from a native object generator (e.g. [13, 50, 59]) which recovers a complete object representation from a single image. The background warp is otherwise preserved, with the reconstructed object mesh also serving as an occluder — blocking background points that should no longer be visible once the camera has orbited past the object. In the single-view setting, WarpHammer densifies the scene cache using only the reference image, the reference scene cache, and a native 3D object generator. The multi-view geometry model introduced next is used only when an auxiliary view is available.

Object reconstruction. We isolate the central object in I_r using an off-the-shelf segmenter, producing masked image I_r^M . We then pass I_r^M together with the corresponding masked region point cloud P_r to SAM3D [13] — an image-to-3D object generator that accepts a point map as conditioning and returns a textured mesh already aligned to it. This native scene-alignment is a key enabler: it removes the need for any post-hoc registration between the reconstructed object and the background warp.

Geometry-focused conditioning. While SAM3D yields reliable shape estimates, its texture and color can deviate from the reference scene’s illumination and appearance. We therefore inject the reconstructed mesh into the cache without donor color: its rendered depth is written into the RGB conditioning buffer $\{R_t\}$, while only its rendered luminance is written into the validity buffer $\{M_t\}$, so that the densified region carries geometric structure and shading cues but no donor-specific color identity. The diffusion prior, conditioned on I_r , then fills in the appearance of these regions, keeping it coherent with the reference scene.

Cache fusion and rendering. We form the fused cache by inserting the densified object into the reference cache,

$$\mathcal{C}_f = \mathcal{C}_r \cup \mathcal{C}_{3D}, \quad \mathcal{C}_{3D} = \{P_{3D}, A_{3D}\}, \quad (2)$$

and resolve visibility during rendering. Because SAM3D natively returns a textured mesh, we render the densified object portion of \mathcal{C}_f from that mesh rather than splatting the sampled P_{3D} as points. Mesh rasterization gives cleaner silhouettes, reliable visibility tests, and — as introduced above — a natural occluder for the original reference points that should no longer be visible after the camera orbits past the object. The warped video $\{R_t\}$ and validity mask $\{M_t\}$ are produced jointly from \mathcal{C}_f and handed to the diffusion prior as in the base pipeline, with the foreground region now densely supported across the full trajectory.

3.3 Extension: Fusing an Auxiliary Object View

Beyond single-image extreme-view synthesis, the object representation from §3.2 also lets WarpHammer incorporate an uncalibrated auxiliary image I_a of the same object, even when it is captured outside the reference scene, e.g., from a catalog, studio image, or web retrieval.

Unlike standard scene-level NVS inputs, I_a has no known pose relative to I_r and may differ in background, lighting, color, or texture. Rather than treating it as a calibrated second view or passing its appearance directly to the model, WarpHammer uses it only as additional *geometric evidence*, coming from unknown viewpoint, while keeping the synthesized appearance anchored to I_r .

Joint geometry from an unposed auxiliary view. We mask the auxiliary image to the object, I_a^M , and pass it, together with the masked reference I_r^M , to a feed-forward multi-view geometry model f_g , instantiated with VGGT [44]:

$$[\Theta_r, \Theta_a, P_r^g, P_a^g] = f_g(I_r^M, I_a^M). \quad (3)$$

The model jointly predicts intrinsics Θ_r, Θ_a and dense object pointmaps P_r^g, P_a^g in a shared coordinate frame, so the auxiliary pointmap arrives already registered to the reference object. We keep confidence-filtered points and transform them into the reference cache’s coordinate frame — P_r and P_r^g describe the same reference-object surface and serve as the alignment anchor between the two frames. Masking the inputs to f_g is important in practice: it focuses the model on object surfaces and stabilizes the predicted relative pose for wide baselines, including hard front-to-back configurations.

Aligned 3D generation with auxiliary support. The auxiliary pointmap enters the densification step as additional conditioning to f_{3D} ,

$$P_{3D} = f_{3D}(I_r, P_r, P_a^g), \quad (4)$$

where P_a^g supplies real evidence for surfaces that are weakly observed or absent from the reference view. The fused cache becomes $\mathcal{C}_f = \mathcal{C}_r \cup \mathcal{C}_{3D} \cup \mathcal{C}_a$, with the auxiliary cache $\mathcal{C}_a = \{P_a^g, A_a\}$ also expressed in the reference frame; rendering and conditioning then proceed exactly as in §3.2.

Appearance-neutral auxiliary conditioning. We apply the same appearance-neutral rendering strategy to the auxiliary view. Rather than passing the auxiliary RGB values to the diffusion prior, we render the aligned auxiliary geometry as a depth-based conditioning cue and use its grayscale luminance as a soft confidence mask. Pixels outside the auxiliary footprint fall back to the reference scene cache with zero auxiliary confidence. Thus, the auxiliary view contributes geometric evidence for missing object surfaces without transferring donor-specific color, texture, or illumination. The precise neutralization and confidence-mask definitions are provided in Sec. A.1.

4 Experiments

We compare WarpHammer against TrajectoryCrafter [54], GEN3C [39], ReCamMaster [4], EX-4D [19], CogNVS [11], SEVA [60], and WorldForge [42], spanning projection-conditioned and camera-conditioned paradigms. We evaluate two variants: a single-view variant and an auxiliary-view variant that additionally consumes an unposed object image from outside the reference scene. To isolate the impact of auxiliary-view conditioning, we extend GEN3C and SEVA to accept a second input view *with known pose from the same scene*, denoted GEN3C-MV and SEVA-MV, and report them as reference-only baselines with GT camera poses.

Benchmarks. We evaluate on five benchmarks spanning synthetic, scanned, and real-world captured data. We introduce **SynView-X**, a benchmark for object-centric NVS under large orbital viewpoint changes, constructed from CAD assets drawn from ShapeNet [9] and Objaverse [14], augmented with scanned objects from GSO [15]. Existing benchmarks do not specifically target extreme orbital deviations around a dominant foreground object. SynView-X fills this gap by providing ground-truth multi-view sequences with controlled large-angle coverage. For scanned and real-world evaluation we use OmniObject3D [48], Co3D [38], Objectron [1], and Mip-NeRF 360 [5]. For each dataset, evaluation pairs are constructed by selecting images with large orbital viewpoint differences; one serves as the reference input and the other as the target view. Dataset details and construction protocol are provided in Sec. B.

Metrics. Our evaluation measures three complementary aspects of performance: image fidelity, geometric accuracy, and perceptual video quality. For image fidelity, we evaluate PSNR, SSIM, and LPIPS on the masked object region at the target viewpoint, and CLIP-F [4] for semantic alignment with the target view, focusing the evaluation on the synthesized object rather than potentially unrelated background (details in Sec. C and Sec. D).

For geometric accuracy, we propose **OrbErr**, a metric tailored to object-centric orbital trajectories. A faithful orbit must satisfy two conditions simultaneously: the camera must follow the intended orbital

viewing direction, and the rendered object must place its visual features at spatial locations consistent with that viewpoint. OrbErr therefore combines two complementary terms:

$$E_{\text{orb}}(t) = \frac{1}{2}E_{\text{euler}}(t) + \frac{1}{2}E_{\text{disp}}(t), \quad (5)$$

where E_{euler} measures normalized wrapped angular deviation in azimuth and elevation from monocular pose estimates [27], and E_{disp} measures object-region feature displacement using mutual nearest-neighbor matches between DINOv2 [35] patch features of the rendered and ground-truth frames. Specifically, nearest neighbors are computed in both directions between the generated and ground-truth object patches, and only reciprocal matches are retained. The displacement of these mutual matches is combined with a coverage penalty, preventing the metric from rewarding methods that match only a small subset of easy patches. Reporting the orbital-angle and feature-displacement terms jointly penalizes partial failures that rotation error or PSNR alone misses, including incorrect object orientation, mirror-like duplications, and incomplete object reconstruction. For compatibility with prior work [4], we also report RotErr, though it is poorly suited to orbital motion (see suppl. C.1). Perceptual video quality is assessed with VBench [20] and reported in the suppl. D.

4.1 Results

Quantitative. Table 1 reports single-view results averaged across all five benchmarks. On image similarity, WarpHammer-GEN3C improves PSNR by 4.2 dB over its GEN3C backbone and by 3.6 dB over the strongest baseline (CogNVS), with consistent gains on SSIM and LPIPS. Camera accuracy tells the same story: WarpHammer-GEN3C reduces rotation error by 50% relative to its backbone, confirming that the densified object conditioning restores the implicit camera cue that scene-only warps lose at extreme viewpoints.

Beyond the single-view setting, WarpHammer enables a capability that no existing scene-level NVS pipeline supports: fusing an unposed auxiliary object view from outside the reference scene. Table 2 reports results in this setting. WarpHammer-GEN3C reaches 14.1 dB PSNR without any ground-truth camera poses or in-scene second views — nearly matching GEN3C-MV at 14.3 dB, which uses GT poses and in-scene views. This validates our key insight: an unposed, out-of-scene image, utilized as geometric evidence rather than as a calibrated view, is nearly as informative as a ground-truth second view with known pose.

Table 1: **Single-view** mean NVS results across 5 datasets (CO3D, Objectron, 360°, OmniObject3D, SynView-X). WarpHammer variants are shaded. Best results in **bold**. **Green** superscripts on PSNR and RotErr indicate improvement over each method’s backbone (TrajCrafter and GEN3C respectively). †OrbErr requires a ground-truth orbital video and is therefore reported only on SynView-X.

Group	Method	Image Similarity			Semantic	Camera Pose		
		PSNR↑	SSIM↑	LPIPS↓	CLIP-F↑	RotErr↓	TransErr↓	OrbErr† ↓
Camera-cond.	ReCamM.	7.91	0.481	0.851	93.42	163.49	0.102	0.3460
Camera-cond.	SEVA	7.68	0.480	0.736	95.10	167.28	0.047	0.2855
Warp-based	EX-4D	7.88	0.464	0.790	95.18	190.15	0.083	0.3192
Warp-based	CogNVS	8.08	0.513	0.768	94.26	176.51	0.063	0.3063
Warp-based	WF	7.64	0.524	0.568	95.73	119.85	0.085	0.3067
Warp-based	TrajCr.	7.58	0.460	0.791	93.62	177.85	0.069	0.3022
Warp-based	GEN3C	7.45	0.416	0.767	94.40	184.10	0.093	0.3058
Ours	WarpHammer-TC	10.79 ^{+3.21}	0.522	0.510	93.25	125.52 ^{-52.33}	0.077	0.2288
Ours	WarpHammer-GEN3C	11.67 ^{+4.22}	0.589	0.444	94.34	91.21 ^{-92.89}	0.024	0.2045

Qualitative. Fig. 3 shows a qualitative comparison along a wide orbital trajectory. Warp-based baselines preserve the input view at small offsets but progressively lose the object as the warp collapses: mirror-like duplications and background leakage dominate at wide angles. Camera-conditioned generation (ReCamMaster) avoids warping artifacts but fails to follow the prescribed orbital trajectory, producing a near-static sequence that barely changes viewpoint. WarpHammer-GEN3C maintains a coherent, identity-preserving rendering across the full orbital range, follows the prescribed camera trajectory, and produces plausible background completion in newly visible regions, a direct consequence of the densified cache providing continuous geometric support where the scene-only warp would otherwise go empty. More qualitative results and animated comparisons can be found in the attached suppl. material.

Table 2: **Auxiliary-view** NVS results average across 5 datasets (CO3D, Objectron, 360°, OmniObject3D, SynView-X). WarpHammer in Shaded row outperforms baselines. Gray methods use GT poses and in-scene second views are shown for reference only. Best results in **bold**.

Setting	Method	Image Similarity			Semantic	Camera Pose	
		PSNR \uparrow	SSIM \uparrow	LPIPS \downarrow	CLIP-F \uparrow	RotErr \downarrow	TransErr \downarrow
GT poses	SEVA-MV	14.60	0.705	0.389	94.61	193.04	0.040
GT poses	GEN3C-MV	14.31	0.696	0.446	93.06	176.96	0.069
No GT poses	SEVA-MV	10.56	0.513	0.519	92.89	97.13	0.050
No GT poses	GEN3C-MV	9.97	0.502	0.546	93.30	81.38	0.088
Ours	WarpHammer-GEN3C	14.09	0.635	0.389	94.84	80.03	0.035

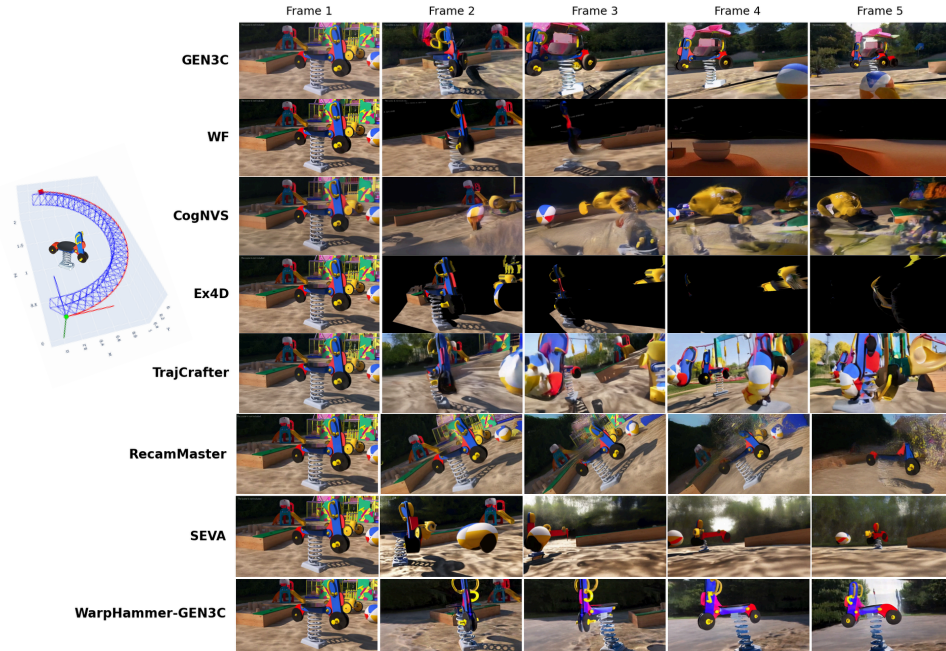


Figure 3: **Qualitative comparison along an extreme orbital trajectory.** Single view NVS. Left: the target camera follows a wide arc around the central object (red curve). Right: five frames sampled from small to extreme orbital offsets. Warp-based methods collapse at large angles; camera-conditioned generation fails to follow the trajectory; WarpHammer-GEN3C renders the object faithfully across the full range.

4.2 Ablation

We ablate the two core components of WarpHammer on 50 SynView-X samples: the object-centric 3D prior and the VGGT-based multi-view fusion. We study four variants across two settings: *Single-view Full*, vs. *w/o 3D prior*, and *Auxiliary-view Full*, vs. *w/o VGGT*. Results are reported in Tab. 3.

Effect of the 3D prior (single-view). Removing the explicit 3D object reconstruction (*Single-view w/o 3D prior*) sharply degrades both image fidelity and camera accuracy simultaneously, confirming that the 3D prior serves a dual role: it supplies the missing surface geometry for newly visible object regions, and restores the implicit camera cue that the warp normally carries but loses when it goes sparse at extreme angles.

Effect of auxiliary-view fusion (VGGT). Comparing *Aux-view Full* against *Aux-view w/o VGGT* isolates the contribution of VGGT-based geometric alignment between the auxiliary view and the reference scene. Even without VGGT, SAM3D still produces a plausible object shape — so 3D content is available in both cases. What VGGT provides is the joint alignment that places the

reconstructed object consistently inside the scene coordinate frame. Without it, the orbital trajectory drifts relative to the object even though its shape is plausible, confirming that aligned conditioning, not 3D content alone, is the critical ingredient for orbital fidelity.

Table 3: Ablation study on SynView-X (n=50). Best results per setting in **bold**.

Setting	Variant	Image Similarity			Semantic	Camera Pose		
		PSNR \uparrow	SSIM \uparrow	LPIPS \downarrow	CLIP-F \uparrow	RotErr \downarrow	TransErr \downarrow	OrbErr \downarrow
Aux-view	Full	16.69	0.560	0.368	94.94	25.36	0.134	0.132
Aux-view	w/o VGGT	9.80	0.360	0.609	94.83	49.37	0.154	0.192
Single-view	Full	12.06	0.468	0.482	94.50	31.05	0.132	0.1338
Single-view	w/o 3D prior	10.05	0.360	0.600	94.84	49.45	0.154	0.1772

5 Summary and Conclusions

WarpHammer addresses a key limitation of projection-conditioned NVS: under large viewpoint changes, the scene warp becomes sparse around the foreground object, weakening both the geometric support and the implicit camera cue provided to the generator. We overcome this by densifying the warped conditioning signal with an explicit object-centric 3D reconstruction, improving PSNR by up to 4.2 dB and reducing rotation error by 50% over strong baselines, without any fine-tuning.

The resulting representation also opens a practical new use case for NVS: incorporating an unposed, out-of-scene auxiliary image of the object, such as a catalog, studio, or retrieved web image. WarpHammer separates geometry from appearance and uses the auxiliary input only as additional structural evidence, while preserving the color, texture, lighting, and scene context of the reference image. We further formalize and evaluate this auxiliary-view setting through a new benchmark designed to test unposed object-centric NVS. Across synthetic, scanned, and real-world benchmarks, our results show that object-centric geometry completion is an effective path toward more robust, flexible, and practically usable NVS systems.

Limitations. WarpHammer relies on accurate object segmentation and the quality of the external 3D reconstruction; segmentation failures or incorrect geometry propagate into the synthesized views. The method is most effective for scenes with a dominant foreground object and may be less reliable for cluttered scenes, thin structures, or transparent materials. The auxiliary-view setting is sensitive to geometric ambiguities when the auxiliary and reference views are either nearly identical or highly dissimilar. Finally, adding a 3D object generator to the pipeline increases inference time relative to the base backbone, which may be a consideration in latency-sensitive applications.

References

- [1] Adel Ahmadyan, Liangkai Zhang, Artsiom Ablavatski, Jianing Wei, and Matthias Grundmann. Objectron: A large scale dataset of object-centric videos in the wild with pose annotations. In *Proceedings of the IEEE/CVF conference on computer vision and pattern recognition*, pages 7822–7831, 2021. [6](#), [16](#)
- [2] Sherwin Bahmani, Ivan Skorokhodov, Guocheng Qian, Aliaksandr Siarohin, Willi Menapace, Andrea Tagliasacchi, David B. Lindell, and Sergey Tulyakov. AC3D: Analyzing and improving 3d camera control in video diffusion transformers. In *Proceedings of the IEEE/CVF Conference on Computer Vision and Pattern Recognition*, 2025. [3](#)
- [3] Sherwin Bahmani, Ivan Skorokhodov, Aliaksandr Siarohin, Willi Menapace, Guocheng Qian, Michael Vasilkovsky, Hsin-Ying Lee, Chaoyang Wang, Jiaxu Zou, Andrea Tagliasacchi, David B. Lindell, and Sergey Tulyakov. VD3D: Taming large video diffusion transformers for 3d camera control. In *International Conference on Learning Representations*, 2025. [3](#)
- [4] Jianhong Bai, Menghan Xia, Xiao Fu, Xintao Wang, Lianrui Mu, Jinwen Cao, Zuozhu Liu, Haoji Hu, Xiang Bai, Pengfei Wan, et al. Recammaster: Camera-controlled generative rendering from a single video. In *Proceedings of the IEEE/CVF International Conference on Computer Vision*, pages 14834–14844, 2025. [6](#), [7](#)
- [5] Jonathan T. Barron, Ben Mildenhall, Dor Verbin, Pratul P. Srinivasan, and Peter Hedman. Mip-nerf 360: Unbounded anti-aliased neural radiance fields. In *Proceedings of the IEEE/CVF Conference on Computer Vision and Pattern Recognition (CVPR)*, pages 5470–5479, 2022. [3](#), [6](#), [16](#)
- [6] Andreas Blattmann, Tim Dockhorn, Sumith Kulal, Daniel Mendelevitch, Maciej Kilian, Dominik Lorenz, Yam Levi, Zion English, Vikram Voleti, Adam Letts, et al. Stable video diffusion: Scaling latent video diffusion models to large datasets. *arXiv preprint arXiv:2311.15127*, 2023. [1](#)
- [7] Chenjie Cao, Chaohui Yu, Shang Liu, Fan Wang, Xiangyang Xue, and Yanwei Fu. MV-GenMaster: Scaling multi-view generation from any image via 3D priors enhanced diffusion model. In *IEEE/CVF Conference on Computer Vision and Pattern Recognition (CVPR)*, 2025. [arXiv:2411.16157](#). [2](#)
- [8] Wei Cao, Hao Zhang, Fengrui Tian, Yulun Wu, Yingying Li, Shenlong Wang, Ning Yu, and Yaoyao Liu. Freeorbit4d: Training-free arbitrary camera redirection for monocular videos via geometry-complete 4d reconstruction. 2026. [4](#)
- [9] Angel X Chang, Thomas Funkhouser, Leonidas Guibas, Pat Hanrahan, Qixing Huang, Zimo Li, Silvio Savarese, Manolis Savva, Shuran Song, Hao Su, et al. Shapenet: An information-rich 3d model repository. *arXiv preprint arXiv:1512.03012*, 2015. [6](#), [16](#)
- [10] Haoxin Chen, Menghan Xia, Yingqing He, Yong Zhang, Xiaodong Cun, Shaoshu Yang, Jinbo Xing, Yaofang Liu, Qifeng Chen, Xintao Wang, Chao Weng, and Ying Shan. VideoCrafter1: Open diffusion models for high-quality video generation. *arXiv preprint arXiv:2310.19512*, 2023. [1](#)
- [11] Kaihua Chen, Tarasha Khurana, and Deva Ramanan. Reconstruct, inpaint, test-time finetune: Dynamic novel-view synthesis from monocular videos. In *Advances in Neural Information Processing Systems*, 2025. [4](#), [6](#)
- [12] Luxi Chen, Zihan Zhou, Min Zhao, Yikai Wang, Ge Zhang, Wenhao Huang, Hao Sun, Ji-Rong Wen, and Chongxuan Li. FlexWorld: Progressively expanding 3D scenes for flexible-view synthesis. *arXiv preprint arXiv:2503.13265*, 2025. [2](#)
- [13] Xingyu Chen, Fu-Jen Chu, Pierre Gleize, Kevin J Liang, Alexander Sax, Hao Tang, Weiyao Wang, Michelle Guo, Thibaut Hardin, Xiang Li, et al. Sam 3d: 3dfy anything in images. *arXiv preprint arXiv:2511.16624*, 2025. [5](#)

- [14] Matt Deitke, Dustin Schwenk, Jordi Salvador, Luca Weihs, Oscar Michel, Eli VanderBilt, Ludwig Schmidt, Kiana Ehsani, Aniruddha Kembhavi, and Ali Farhadi. Objaverse: A universe of annotated 3d objects. In *Proceedings of the IEEE/CVF conference on computer vision and pattern recognition*, pages 13142–13153, 2023. 6, 16
- [15] Laura Downs, Anthony Francis, Nate Koenig, Brandon Kinman, Ryan Hickman, Krista Reymann, Thomas B McHugh, and Vincent Vanhoucke. Google scanned objects: A high-quality dataset of 3d scanned household items. In *2022 International Conference on Robotics and Automation (ICRA)*, pages 2553–2560. Ieee, 2022. 6, 16
- [16] Ruiqi Gao, Aleksander Holynski, Philipp Henzler, Arthur Brussee, Ricardo Martin-Brualla, Pratul Srinivasan, Jonathan T. Barron, and Ben Poole. CAT3D: Create anything in 3D with multi-view diffusion models. In *Advances in Neural Information Processing Systems (NeurIPS)*, 2024. arXiv:2405.10314. 1
- [17] Hao He, Yinghao Xu, Yuwei Guo, Gordon Wetzstein, Bo Dai, Hongsheng Li, and Ceyuan Yang. CameraCtrl: Enabling camera control for text-to-video generation. *arXiv preprint arXiv:2404.02101*, 2024. 3
- [18] Hao He, Ceyuan Yang, Shanchuan Lin, Yinghao Xu, Meng Wei, Liangke Gui, Qi Zhao, Gordon Wetzstein, Lu Jiang, and Hongsheng Li. CameraCtrl II: Dynamic scene exploration via camera-controlled video diffusion models. In *Proceedings of the IEEE/CVF International Conference on Computer Vision*, 2025. 3
- [19] Tao Hu, Haoyang Peng, Xiao Liu, and Yuewen Ma. EX-4D: Extreme viewpoint 4D video synthesis via depth watertight mesh. *arXiv preprint arXiv:2506.05554*, 2025. 2, 4, 6
- [20] Ziqi Huang, Yinan He, Jiashuo Yu, Fan Zhang, Chenyang Si, Yuming Jiang, Yuanhan Zhang, Tianxing Wu, Qingyang Jin, Nattapol Chanpaisit, et al. Vbench: Comprehensive benchmark suite for video generative models. In *Proceedings of the IEEE/CVF Conference on Computer Vision and Pattern Recognition*, pages 21807–21818, 2024. 7, 19
- [21] Hanwen Jiang, Hao Tan, Peng Wang, Haiyan Jin, Yue Zhao, Sai Bi, Kai Zhang, Fujun Luan, Kalyan Sunkavalli, Qixing Huang, and Georgios Pavlakos. RayZer: A self-supervised large view synthesis model. *arXiv preprint arXiv:2505.00702*, 2025. 1
- [22] Zeyinzi Jiang, Zhen Han, Chaojie Mao, Jingfeng Zhang, Yulin Pan, and Yu Liu. Vace: All-in-one video creation and editing. In *Proceedings of the IEEE/CVF International Conference on Computer Vision*, pages 17191–17202, 2025. 4
- [23] Haiyan Jin, Hanwen Jiang, Hao Tan, Kai Zhang, Sai Bi, Tianyuan Zhang, Fujun Luan, Noah Snavely, and Zexiang Xu. LVSM: A large view synthesis model with minimal 3D inductive bias. In *International Conference on Learning Representations (ICLR)*, 2025. arXiv:2410.17242. 1
- [24] Bernhard Kerbl, Georgios Kopanas, Thomas Leimkühler, and George Drettakis. 3d gaussian splatting for real-time radiance field rendering. *ACM Transactions on Graphics*, 42(4):1–14, 2023. 3
- [25] Teng Li, Guangcong Zheng, Rui Jiang, Shuigen Zhan, Tao Wu, Yehao Lu, Yining Lin, and Xi Li. RealCam-I2V: Real-world image-to-video generation with interactive complex camera control. In *Proceedings of the IEEE/CVF International Conference on Computer Vision*, pages 28785–28796, 2025. 3
- [26] Jinglin Liang, Zijian Zhou, Rui Huang, Shuangping Huang, and Yichen Gong. Orbitnvs: Harnessing video diffusion priors for novel view synthesis. *arXiv preprint arXiv:2603.19613*, 2026. 1
- [27] Haotong Lin, Sili Chen, Junhao Liew, Donny Y Chen, Zhenyu Li, Guang Shi, Jiashi Feng, and Bingyi Kang. Depth anything 3: Recovering the visual space from any views. *arXiv preprint arXiv:2511.10647*, 2025. 7
- [28] Ruoshi Liu, Rundi Wu, Basile Van Hoorick, Pavel Tokmakov, Sergey Zakharov, and Carl Vondrick. Zero-1-to-3: Zero-shot one image to 3d object. In *Proceedings of the IEEE/CVF International Conference on Computer Vision*, pages 9298–9309, 2023. 1, 3

- [29] Xi Liu, Chaoyi Zhou, and Siyu Huang. 3DGS-enhancer: Enhancing unbounded 3D gaussian splatting with view-consistent 2D diffusion priors. In *Advances in Neural Information Processing Systems (NeurIPS)*, 2024. arXiv:2410.16266. 2
- [30] Yuan Liu, Cheng Lin, Zijiao Zeng, Xiaoxiao Long, Lingjie Liu, Taku Komura, and Wenping Wang. SyncDreamer: Generating multiview-consistent images from a single-view image. In *International Conference on Learning Representations*, 2024. 1, 3
- [31] Xiaoxiao Long, Yuan-Chen Guo, Cheng Lin, Yuan Liu, Zhiyang Dou, Lingjie Liu, Yuexin Ma, Song-Hai Zhang, Marc Habermann, Christian Theobalt, and Wenping Wang. Wonder3D: Single image to 3d using cross-domain diffusion. In *Proceedings of the IEEE/CVF Conference on Computer Vision and Pattern Recognition*, 2024. 1, 3
- [32] Yawen Luo, Jianhong Bai, Xiaoyu Shi, Menghan Xia, Xintao Wang, Pengfei Wan, Di Zhang, Kun Gai, and Tianfan Xue. CamCloneMaster: Enabling reference-based camera control for video generation. *arXiv preprint arXiv:2506.03140*, 2025. 3
- [33] Baorui Ma, Huachen Gao, Haoge Deng, Zhengxiong Luo, Tiejun Huang, Lulu Tang, and Xinlong Wang. You see it, you got it: Learning 3D creation on pose-free videos at scale. In *IEEE/CVF Conference on Computer Vision and Pattern Recognition (CVPR)*, 2025. arXiv:2412.06699. 2
- [34] Ben Mildenhall, Pratul P. Srinivasan, Matthew Tancik, Jonathan T. Barron, Ravi Ramamoorthi, and Ren Ng. NeRF: Representing scenes as neural radiance fields for view synthesis. In *European Conference on Computer Vision*, pages 405–421. Springer, 2020. 3
- [35] Maxime Oquab, Timothée Darcet, Théo Moutakanni, Huy Vo, Marc Szafraniec, Vasil Khalidov, Pierre Fernandez, Daniel Haziza, Francisco Massa, Alaaeldin El-Nouby, et al. Dinov2: Learning robust visual features without supervision. *arXiv preprint arXiv:2304.07193*, 2023. 7, 18
- [36] Dustin Podell, Zion English, Kyle Lacey, Andreas Blattmann, Tim Dockhorn, Jonas Müller, Joe Penna, and Robin Rombach. SDXL: Improving latent diffusion models for high-resolution image synthesis. In *International Conference on Learning Representations (ICLR)*, 2024. 1
- [37] Nikhila Ravi, Valentin Gabeur, Yuan-Ting Hu, Ronghang Hu, Chaitanya Ryali, Tengyu Ma, Haitham Khedr, Roman Rädle, Chloe Rolland, Laura Gustafson, et al. Sam 2: Segment anything in images and videos. *arXiv preprint arXiv:2408.00714*, 2024. 18
- [38] Jeremy Reizenstein, Roman Shapovalov, Philipp Henzler, Luca Sbordone, Patrick Labatut, and David Novotny. Common objects in 3d: Large-scale learning and evaluation of real-life 3d category reconstruction. In *Proceedings of the IEEE/CVF international conference on computer vision*, pages 10901–10911, 2021. 6, 16
- [39] Xuanchi Ren, Tianchang Shen, Jiahui Huang, Huan Ling, Yifan Lu, Merlin Nimier-David, Thomas Müller, Alexander Keller, Sanja Fidler, and Jun Gao. Gen3c: 3d-informed world-consistent video generation with precise camera control. In *Proceedings of the IEEE/CVF Conference on Computer Vision and Pattern Recognition*, pages 6121–6132, 2025. 2, 3, 4, 6
- [40] Robin Rombach, Andreas Blattmann, Dominik Lorenz, Patrick Esser, and Björn Ommer. High-resolution image synthesis with latent diffusion models. In *IEEE/CVF Conference on Computer Vision and Pattern Recognition (CVPR)*, 2022. 1
- [41] Ido Sobol, Chenfeng Xu, and Or Litany. Zero-to-hero: Enhancing zero-shot novel view synthesis via attention map filtering. *Advances in Neural Information Processing Systems*, 37: 30522–30553, 2024. 3
- [42] Chenxi Song, Yanming Yang, Tong Zhao, Ruibo Li, and Chi Zhang. WorldForge: Unlocking emergent 3d/4d generation in video diffusion model via training-free guidance. *arXiv preprint arXiv:2509.15130*, 2025. 3, 6
- [43] Vikram Voleti, Chun-Han Yao, Mark Boss, Adam Letts, David Pankratz, Dmitry Tochilkin, Christian Laforte, Robin Rombach, and Varun Jampani. SV3D: Novel multi-view synthesis and 3d generation from a single image using latent video diffusion. In *European Conference on Computer Vision*, 2024. 3

- [44] Jianyuan Wang, Minghao Chen, Nikita Karaev, Andrea Vedaldi, Christian Rupprecht, and David Novotny. Vggt: Visual geometry grounded transformer. In *Proceedings of the Computer Vision and Pattern Recognition Conference*, pages 5294–5306, 2025. 6
- [45] Qianqian Wang, Zhicheng Wang, Kyle Genova, Pratul P. Srinivasan, Howard Zhou, Jonathan T. Barron, Ricardo Martin-Brualla, Noah Snively, and Thomas Funkhouser. IBRNet: Learning multi-view image-based rendering. In *Proceedings of the IEEE/CVF Conference on Computer Vision and Pattern Recognition*, pages 4690–4699, 2021. 3
- [46] Zhouxia Wang, Ziyang Yuan, Xintao Wang, Tianshui Chen, Menghan Xia, Ping Luo, and Ying Shan. MotionCtrl: A unified and flexible motion controller for video generation. In *ACM SIGGRAPH Conference Papers*, 2024. 3
- [47] Rundi Wu, Ruiqi Gao, Ben Poole, Alex Trevithick, Changxi Zheng, Jonathan T. Barron, and Aleksander Holynski. CAT4D: Create anything in 4D with multi-view video diffusion models. In *IEEE/CVF Conference on Computer Vision and Pattern Recognition (CVPR)*, 2025. arXiv:2411.18613. 1
- [48] Tong Wu, Jiarui Zhang, Xiao Fu, Yuxin Wang, Jiawei Ren, Liang Pan, Wayne Wu, Lei Yang, Jiaqi Wang, Chen Qian, et al. Omniobject3d: Large-vocabulary 3d object dataset for realistic perception, reconstruction and generation. In *Proceedings of the IEEE/CVF conference on computer vision and pattern recognition*, pages 803–814, 2023. 6, 16
- [49] Zirui Wu, Zeren Jiang, Martin R. Oswald, and Jie Song. From rays to projections: Better inputs for feed-forward view synthesis. *arXiv preprint arXiv:2601.05116*, 2026. 2
- [50] Jianfeng Xiang, Zelong Lv, Sicheng Xu, Yu Deng, Ruicheng Wang, Bowen Zhang, Dong Chen, Xin Tong, and Jiaolong Yang. Structured 3d latents for scalable and versatile 3d generation. In *Proceedings of the IEEE/CVF conference on computer vision and pattern recognition*, pages 21469–21480, 2025. 5
- [51] Yiming Xie, Chun-Han Yao, Vikram Voleti, Huaizu Jiang, and Varun Jampani. SV4D: Dynamic 3d content generation with multi-frame and multi-view consistency. In *International Conference on Learning Representations*, 2025. 3
- [52] Yunzhi Yan, Zhen Xu, Haotong Lin, Haian Jin, Haoyu Guo, Yida Wang, Kun Zhan, Xianpeng Lang, Hujun Bao, Xiaowei Zhou, and Sida Peng. StreetCrafter: Street view synthesis with controllable video diffusion models. In *IEEE/CVF Conference on Computer Vision and Pattern Recognition (CVPR)*, 2025. arXiv:2412.13188. 2
- [53] Alex Yu, Vickie Ye, Matthew Tancik, and Angjoo Kanazawa. pixelNeRF: Neural radiance fields from one or few images. In *Proceedings of the IEEE/CVF Conference on Computer Vision and Pattern Recognition*, pages 4578–4587, 2021. 3
- [54] Mark Yu, Wenbo Hu, Jinbo Xing, and Ying Shan. Trajectorycrafter: Redirecting camera trajectory for monocular videos via diffusion models. In *Proceedings of the IEEE/CVF international conference on computer vision*, pages 100–111, 2025. 2, 3, 4, 6
- [55] Wangbo Yu, Jinbo Xing, Li Yuan, Wenbo Hu, Xiaoyu Li, Zhipeng Huang, Xiangjun Gao, Tien-Tsin Wong, Ying Shan, and Yonghong Tian. ViewCrafter: Taming video diffusion models for high-fidelity novel view synthesis. *arXiv preprint arXiv:2409.02048*, 2024. 2, 3
- [56] Songchun Zhang, Huiyao Xu, Sitong Guo, Zhongwei Xie, Pengwei Liu, Hujun Bao, Weiwei Xu, and Changqing Zou. SpatialCrafter: Unleashing the imagination of video diffusion models for scene reconstruction from limited observations. In *Proceedings of the IEEE/CVF International Conference on Computer Vision*, pages 27794–27805, 2025. 3
- [57] Xiang Zhang, Yang Zhang, Lukas Mehl, Markus Gross, and Christopher Schroers. High-fidelity novel view synthesis via splatting-guided diffusion. *arXiv preprint arXiv:2502.12752*, 2025. 2
- [58] Yuqi Zhang, Guanying Chen, Jiaying Chen, Chuanyu Fu, Chuan Huang, and Shuguang Cui. CloseUpShot: Close-up novel view synthesis from sparse-views via point-conditioned diffusion model. *arXiv preprint arXiv:2511.13121*, 2025. 2

- [59] Zibo Zhao, Zeqiang Lai, Qingxiang Lin, Yunfei Zhao, Haolin Liu, Shuhui Yang, Yifei Feng, Mingxin Yang, Sheng Zhang, Xianghui Yang, et al. Hunyuan3d 2.0: Scaling diffusion models for high resolution textured 3d assets generation. *arXiv preprint arXiv:2501.12202*, 2025. 5
- [60] Jensen Zhou, Hang Gao, Vikram Voleti, Aaryaman Vasishtha, Chun-Han Yao, Mark Boss, Philip Torr, Christian Rupprecht, and Varun Jampani. Stable virtual camera: Generative view synthesis with diffusion models. In *Proceedings of the IEEE/CVF International Conference on Computer Vision*, pages 12405–12414, 2025. 1, 3, 6
- [61] Zhizhuo Zhou and Shubham Tulsiani. SparseFusion: Distilling view-conditioned diffusion for 3d reconstruction. In *Proceedings of the IEEE/CVF Conference on Computer Vision and Pattern Recognition*, 2023. 3

Supplementary Material: WarpHammer

In this supplementary material, we provide additional details on implementation, datasets, evaluation metrics, and further quantitative and qualitative results.

A Implementation Details

A.1 Appearance-Neutral Auxiliary Conditioning

In the main paper, we condition the diffusion prior on an appearance-neutralized version of the auxiliary rendering rather than its raw RGB. We provide here the precise definitions of the neutralized buffer and the associated confidence mask.

Motivation. The auxiliary view is geometrically aligned with the reference scene but originates from a donor object that generally differs in color, texture, and illumination. Passing its RGB directly to the diffusion model would encourage the generator to copy these donor-specific cues, driving the synthesized object away from the appearance expected from the reference scene. We therefore retain the geometric information carried by the auxiliary view while suppressing its appearance signature.

Neutralized buffer and confidence mask. Let R_t^a denote the auxiliary RGB rendering at target frame t , D_t^a the corresponding auxiliary depth rendering, R_t^s the rendering from the reference scene cache, and Ω_t^a the rendered auxiliary object footprint. We define the neutralized auxiliary buffer \tilde{R}_t^a and a soft confidence mask M_t^a jointly as

$$(\tilde{R}_t^a(u, v), M_t^a(u, v)) = \begin{cases} (g(D_t^a(u, v)), h(R_t^a(u, v))), & (u, v) \in \Omega_t^a, \\ (R_t^s(u, v), 0), & \text{otherwise.} \end{cases} \quad (6)$$

Here, $g(\cdot)$ converts the auxiliary depth rendering into an appearance-neutral RGB conditioning signal, and $h(\cdot)$ converts the auxiliary RGB rendering into a soft confidence value.

Implementation. We normalize the rendered auxiliary depth over the auxiliary footprint:

$$\bar{D}_t^a(u, v) = \frac{D_t^a(u, v) - \min_{(u', v') \in \Omega_t^a} D_t^a(u', v')}{\max_{(u', v') \in \Omega_t^a} D_t^a(u', v') - \min_{(u', v') \in \Omega_t^a} D_t^a(u', v') + \epsilon}, \quad (7)$$

where ϵ is a small constant for numerical stability. The neutralization function g repeats this normalized scalar depth value across the RGB channels:

$$g(D_t^a(u, v)) = (\bar{D}_t^a(u, v), \bar{D}_t^a(u, v), \bar{D}_t^a(u, v)). \quad (8)$$

Thus, \tilde{R}_t^a provides a depth-based geometry cue without transferring donor-specific color or texture.

The confidence function h is computed as the grayscale luminance of the auxiliary RGB rendering:

$$h(R_t^a(u, v)) = 0.299 R_{t,r}^a(u, v) + 0.587 R_{t,g}^a(u, v) + 0.114 R_{t,b}^a(u, v), \quad (9)$$

with values clipped to $[0, 1]$ if needed. Therefore, M_t^a acts as a soft per-pixel validity mask: it is high on well-rendered, visible auxiliary object regions and zero outside the auxiliary footprint. This formulation allows the auxiliary view to contribute object layout and geometry while preventing the diffusion prior from copying its donor-specific color, texture, or illumination.

Implementation. In our implementation, both g and h are luminance-based. The neutralization g is a grayscale projection of the auxiliary rendering, which strips donor-specific color identity while preserving shading and silhouette structure. The confidence h is taken as the luminance of the pre-neutralized rendering, yielding a smooth signal that is high on well-illuminated, well-supported surfaces and low on poorly observed or near-silhouette regions. Outside the auxiliary footprint Ω_t^a , the buffer falls back to the reference scene cache and the mask is zero, so the diffusion prior receives no auxiliary signal in those regions. The auxiliary view thus guides the generated object’s layout and geometry without forcing the model to inherit its color or texture.

B Dataset Details

B.1 Dataset Creation

For each benchmark, we construct evaluation pairs by selecting two views of the same object (or scene) separated by a large orbital offset. The first view serves as the *reference* input, the second as the auxiliary target, and a sequence of intermediate frames provides the ground-truth orbital video. All camera poses are converted to a common OpenCV world-to-camera convention. The dataset-specific selection and pre-processing protocols are described below.

CO3D [38] (160 pairs). For each sequence, we greedily select up to 20 pairs that maximize frame separation while satisfying $|\text{yaw}| \in [100^\circ, 190^\circ]$ and $|\text{pitch}| \leq 40^\circ$. Pairs are further filtered by foreground-mask coverage in $[5\%, 95\%]$ using the segmentation masks provided with CO3D. The ground-truth orbital video consists of the ordered real frames lying between the two selected views.

Mip-NeRF 360 [5] (57 pairs). Camera poses are taken from the COLMAP reconstructions provided with the dataset, and the dense scene point cloud is used to estimate the 3D scene centre, which serves as the per-view crop anchor. Foreground masks are extracted by an off-the-shelf saliency segmentation model and made cross-view consistent by projecting the foreground 3D points from one view into the other and retaining only mask components that overlap with these projections. Intermediate ground-truth frames are obtained by traversing the shorter azimuthal arc between the two selected cameras.

OmniObject3D [48] (500 pairs). We use the rendered images and camera poses provided by OmniObject3D. For each object, a pair satisfying our orbital-rotation criteria is sampled at random from all qualifying combinations. The reference view is composited onto a randomly sampled perspective crop from an HDRI panorama to simulate a realistic background, while the auxiliary view is placed on a white background, yielding the unposed object input used by WarpHammer. Ground-truth video frames are taken as the rendered frames closest, in spherical distance, to a linearly interpolated arc between the two selected views.

Objectron [1] (9 pairs). We decode the original sequences and convert their camera transforms to our common OpenCV convention. Per sequence, we select the pair with the largest in-range $|\text{yaw}|$, prioritizing pairs whose annotated 3D bounding box is well-framed. Foreground masks are obtained from an off-the-shelf saliency model, and intermediate frames are taken directly from the source monocular videos.

SynView-X (900 pairs). SynView-X aggregates synthetic and scanned assets rendered to support extreme orbital viewpoint changes. It is composed of 777 pairs from ShapeNetCore [9], 20 pairs from GSO [15], 103 pairs from Objaverse [14]. The ShapeNet, GSO, and Objaverse assets are rendered offline; for ShapeNet and GSO, yaw and pitch are sampled deterministically per asset to ensure reproducibility, with the orbit direction matching the conditioning convention used by GEN3C so that the stored angles can be passed directly as conditioning signals. Together, these subsets cover man-made objects, real-scanned assets, and procedurally generated scenes, giving SynView-X the diversity needed to stress-test extreme-viewpoint synthesis under controlled conditions.

Pair-selection summary. Across all five benchmarks, evaluation pairs lie on an orbital arc around the object of interest, with yaw separation in $[100^\circ, 190^\circ]$ and bounded pitch. The reference view is provided as input to all methods, the auxiliary view is used as the unposed conditioning input for WarpHammer auxiliary-view variants. Intermediate frames define the ground-truth orbital video for video-quality and OrbErr computation.

C Evaluation Metrics Details

C.1 Orbital Evaluation: Limitations of RotErr and Definition of OrbErr

The standard relative rotation error

$$E_{\text{rot}}(t) = \cos^{-1} \left(\frac{\text{tr}(\hat{R}_t R_t^\top) - 1}{2} \right) \quad (10)$$

measures the geodesic distance on $\text{SO}(3)$ between the predicted and ground-truth rotation matrices. This is a useful metric for general camera-control evaluation, but it is not fully aligned with object-centric orbital novel view synthesis. In our setting, the desired motion is primarily defined by the orbital viewpoint around the object, i.e., its azimuth and elevation, rather than by an arbitrary 3D rotation.

Conflation of orbital and non-orbital errors. RotErr collapses all rotational degrees of freedom into a single scalar and does not distinguish whether the error originates in azimuth, elevation, or in-plane roll. Azimuth and elevation determine the object-centric viewpoint, while roll changes the image-plane orientation without necessarily changing the orbital position around the object. Concretely, consider two predictions with the same geodesic rotation error:

1. $\hat{R}_t^{(1)}$: azimuth error of 30° , with no elevation or roll error.
2. $\hat{R}_t^{(2)}$: roll error of 30° , with no azimuth or elevation error.

Both yield $E_{\text{rot}}(t) = 30^\circ$, yet they represent different failure modes: the first observes the object from the wrong orbital viewpoint, while the second preserves the orbital direction but introduces an in-plane rotation. For object-centric orbital synthesis, these errors should not be treated as equivalent. In Figure 4, we illustrate such a failure case: GEN3C achieves a low rotation error under large viewpoint changes, yet the car orientation is incorrect, indicating that the metric fails to capture this error.

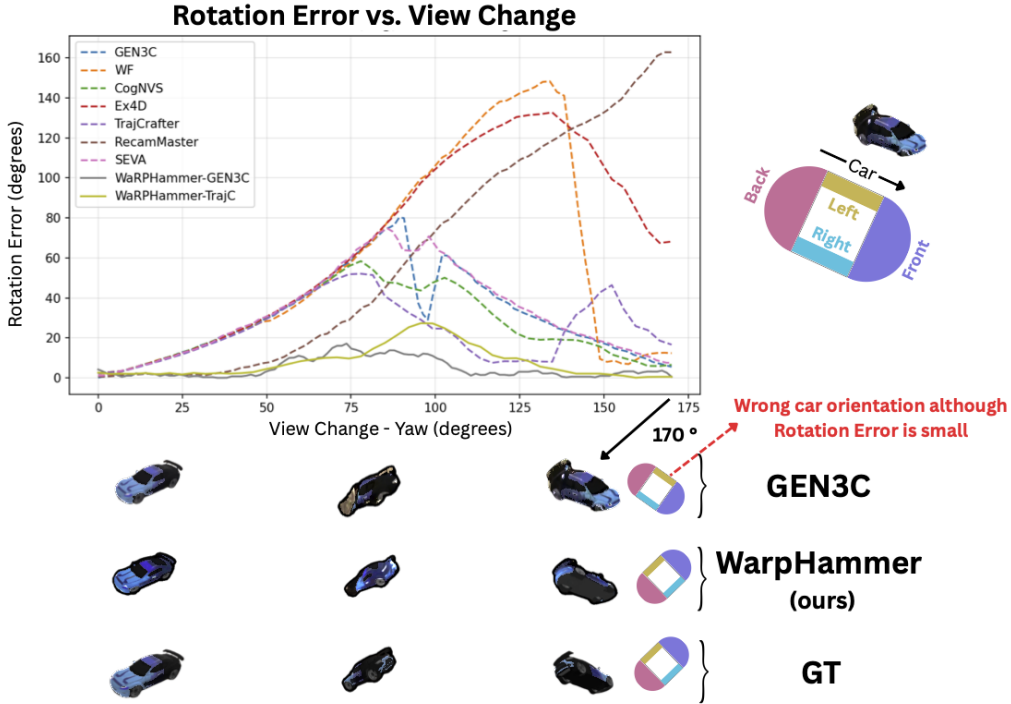


Figure 4: **Rotation error vs. view change.** Despite decreasing rotation error at large viewpoint changes, the predicted object orientation can still be incorrect (see comparison with GT), indicating that rotation error alone is insufficient for evaluating object-centric consistency in orbital settings.

Insensitivity to orbital position. RotErr depends only on rotation matrices and ignores camera translation entirely. Even if rotation is perfectly recovered, a camera centre that lies off the intended orbital arc is not penalized. Conversely, under monocular pose estimation, absolute translation is unrecoverable up to scale, so naively reporting translation error is unreliable. A metric tailored to orbital fidelity must therefore evaluate the orbital viewpoint without depending on metric translation.

OrbErr. We introduce OrbErr, a metric designed for object-centric orbital evaluation. OrbErr combines two complementary terms: (i) a rotation-derived Euler-angle error that measures azimuth and elevation agreement, and (ii) a feature-displacement error that checks whether object features appear at their expected spatial positions in the generated frame. This allows the metric to penalize cases where the camera estimate appears plausible but the object is rendered from an incorrect orbital viewpoint.

Given monocular pose estimates $\{\hat{R}_t\}_{t=0}^T$ and target rotations $\{R_t\}_{t=0}^T$, we first compute rotations relative to the initial frame:

$$\hat{R}_t^{\text{rel}} = \hat{R}_t \hat{R}_0^\top, \quad R_t^{\text{rel}} = R_t R_0^\top. \quad (11)$$

We extract the camera forward direction as the third row of the relative rotation,

$$\hat{f}_t = e_3^\top \hat{R}_t^{\text{rel}}, \quad f_t = e_3^\top R_t^{\text{rel}}, \quad \hat{f}_t, f_t \in \mathbb{R}^3, \quad (12)$$

and decompose it into azimuth and elevation:

$$\hat{\theta}_t = \text{atan2}(\hat{f}_{t,x}, \hat{f}_{t,z}), \quad \theta_t = \text{atan2}(f_{t,x}, f_{t,z}), \quad (13)$$

$$\hat{\phi}_t = \text{atan2}\left(-\hat{f}_{t,y}, \sqrt{\hat{f}_{t,x}^2 + \hat{f}_{t,z}^2}\right), \quad \phi_t = \text{atan2}\left(-f_{t,y}, \sqrt{f_{t,x}^2 + f_{t,z}^2}\right). \quad (14)$$

The wrapped angular distance is

$$d_\angle(a, b) = |\text{atan2}(\sin(a - b), \cos(a - b))|. \quad (15)$$

We define the normalized Euler-angle orbital error as

$$E_{\text{euler}}(t) = \frac{1}{2} \frac{d_\angle(\hat{\theta}_t, \theta_t)}{\pi} + \frac{1}{2} \frac{d_\angle(\hat{\phi}_t, \phi_t)}{\pi}. \quad (16)$$

This term measures whether the generated frame corresponds to the intended orbital viewing direction, focusing on azimuth and elevation rather than arbitrary 3D rotation error.

To additionally verify that the rendered object appearance agrees with the intended viewpoint, we compute a feature-displacement error using DINOv2 [35] patch features on a $G \times G$ grid, restricted to object masks obtained from SAM [37]. Unlike a one-sided nearest-neighbor distance, which can match many ground-truth patches to the same generated patch, we use mutual nearest-neighbor matches between the ground-truth and generated object regions.

Let Ω_t^{gt} and Ω_t^{gen} denote the valid object patches in the ground-truth and generated frames, respectively. We ℓ_2 -normalize all DINOv2 patch features and compute nearest neighbors by cosine similarity. For each ground-truth patch $i \in \Omega_t^{\text{gt}}$, let $\text{NN}_{\text{gen}}(i)$ be its nearest generated patch. Similarly, for each generated patch $j \in \Omega_t^{\text{gen}}$, let $\text{NN}_{\text{gt}}(j)$ be its nearest ground-truth patch. The set of mutual nearest-neighbor matches is

$$\mathcal{M}_t = \{(i, j) : j = \text{NN}_{\text{gen}}(i), i = \text{NN}_{\text{gt}}(j)\}. \quad (17)$$

The mutual feature-displacement error is

$$E_{\text{disp}}^{\text{mnn}}(t) = \frac{1}{|\mathcal{M}_t|} \sum_{(i,j) \in \mathcal{M}_t} \frac{\|p_i - p_j\|_2}{\sqrt{2}(G-1)}, \quad (18)$$

where p_i and p_j are the two-dimensional grid coordinates of the matched patches. The normalization by $\sqrt{2}(G-1)$ converts the displacement to units of the grid diagonal.

Because mutual matching may produce a small set of confident matches even when the generated object is incomplete, we also include a coverage penalty:

$$E_{\text{cov}}(t) = 1 - \frac{2|\mathcal{M}_t|}{|\Omega_t^{\text{gt}}| + |\Omega_t^{\text{gen}}|}. \quad (19)$$

The final feature-displacement term is

$$E_{\text{disp}}(t) = \frac{1}{2}E_{\text{disp}}^{\text{mnn}}(t) + \frac{1}{2}E_{\text{cov}}(t). \quad (20)$$

If no mutual matches are found, we set $E_{\text{disp}}(t) = 1$.

The final orbital error averages both components:

$$E_{\text{orb}}(t) = \frac{1}{2}E_{\text{euler}}(t) + \frac{1}{2}E_{\text{disp}}(t). \quad (21)$$

OrbErr therefore evaluates both the estimated orbital viewing direction and the spatial consistency of object features. The mutual nearest-neighbor constraint makes the feature-displacement term more robust to many-to-one matches, repeated textures, and mirror-like duplications, while the coverage penalty discourages incomplete or weakly supported object reconstructions from receiving artificially low error. We use OrbErr as the primary measure of orbital fidelity, while still reporting RotErr for compatibility with prior camera-controlled video generation work.

D Additional Quantitative Results

We provide a per-dataset breakdown of the single-view novel view synthesis benchmark in Table 4, complementing the aggregated results reported in the main paper. The table reports image similarity (PSNR, SSIM, LPIPS), semantic consistency (CLIP-F), camera pose accuracy (RotErr, TransErr), feature matching (MatchPx), and VBench video-quality metrics (TempFlick, SubjCons, BGCons, ImagQual, AesQual, MotSmooth) across the five evaluation datasets: CO3D, Objectron, 360°, OmniObject3D, and Subset-900.

Across image-similarity metrics, WarpHammer achieves the strongest PSNR, SSIM, and LPIPS scores on CO3D, 360°, and Subset-900, and remains competitive on Objectron and OmniObject3D. The camera-pose results show that WarpHammer dramatically reduces rotation error on object-centric data, most notably on Objectron (RotErr 24.98 vs. ≥ 261 for all baselines), while also yielding the lowest translation error on four of the five datasets. Baselines remain competitive on a subset of perceptual VBench metrics (e.g., AesQual, MotSmooth, and consistency scores), where camera-conditioned methods such as SEVA and ReCamMaster benefit from their conservative, near-static synthesis behavior. Overall, the per-dataset results are consistent with the aggregated trends in the main paper and confirm that the gains from object-centric densification generalize across diverse object-centric and scene-level benchmarks.

VBench video-quality analysis. We further evaluate generated videos with the perceptual VBench metrics [20] along three axes: temporal/subject/background consistency, per-frame image quality, and motion smoothness. Table 5 reports the single-view setting and Table 6 the auxiliary-view setting, both averaged across the five datasets.

In the single-view regime, some baselines achieve higher scores on individual VBench metrics. However, these improvements do not necessarily indicate better execution of the intended camera motion: as shown by the OrbErr scores in Table 5, these methods often exhibit substantially larger orbital errors. This is especially evident for camera-conditioned baselines such as SEVA and ReCamMaster, whose favorable VBench scores may be driven by temporal consistency and motion smoothness rather than by accurate viewpoint progression along the target orbit. In contrast, WarpHammer favors trajectory faithfulness while may results lower perceptual scores as generating a genuine large-angle orbit inherently produces more inter-frame variation than methods that do not accurately follow the intended viewpoint progression. This reflects a tension in current video-quality metrics, which can reward temporal consistency and motion smoothness regardless of whether the requested orbit was correctly executed. Within this regime, WarpHammer-GEN3C achieves the lowest OrbErr while remaining competitive on background consistency and motion smoothness, and WarpHammer-TC achieves the best ImagQual score, indicating that object-centric densification preserves both orbital fidelity and per-frame quality under aggressive viewpoint changes.

In the auxiliary-view regime (Table 6), where models that natively support second-view conditioning (GEN3C-MV, SEVA-MV) are evaluated alongside WarpHammer-GEN3C, the picture flips: WarpHammer-GEN3C achieves the best TempFlick, SubjCons, BGCons, and MotSmooth without

using ground-truth poses or in-scene second views, while remaining competitive on ImagQual. This confirms that the gains from object-centric densification translate to perceptual video quality once the same auxiliary information available to multi-view baselines is consumed, and that our improvements are not limited to image- or pose-level metrics.

E Additional Qualitative Results

We present additional qualitative comparisons that complement the main paper. Figure 5 shows novel view synthesis results with auxiliary view, where applicable, from the back of the car showing a full orbital trajectory around a car and comparing all baselines side-by-side with WarpHammer. The example is selected to span a wide range of azimuthal viewpoints, including angles far from the input view, where the differences between methods become most apparent.

Warp-based baselines (TrajectoryCrafter, GEN3C, EX-4D, CogNVS) reproduce the input view faithfully at small offsets but progressively degrade as the orbital angle grows: occluded regions of the car are filled with warped ghost geometry, and large-angle frames frequently exhibit mirror-like duplications of the visible side rather than the genuine far side of the object. Camera-conditioned baselines (ReCamMaster, SEVA) avoid such warping artifacts but instead produce near-static syntheses that fail to follow the prescribed orbital trajectory, so the object viewpoint barely changes across frames. In contrast, WarpHammer produces a coherent orbital sequence in which the car is rendered from the correct viewpoint at each frame, with consistent geometry, plausible far-side appearance, and stable background, demonstrating the benefit of object-centric 3D densification under large viewpoint changes.



Figure 5: Novel view synthesis comparison along a full orbital trajectory around a car. Warp-based baselines exhibit ghosting and mirror-like duplication at large angles, camera-conditioned baselines fail to follow the orbital motion, while WarpHammer produces a coherent, geometry-faithful orbital sequence.

Table 4: Novel view synthesis benchmark results (single-view setting, no multi-view conditioning). \uparrow higher is better, \downarrow lower is better.

Dataset	Metric	TrajCr.	GEN3C	ReCamM.	EX-4D	CogNVS	SEVA	WarpHammer
CO3D	PSNR \uparrow	5.86	6.52	3.92	5.25	5.70	6.42	10.45
	SSIM \uparrow	0.416	0.394	0.407	0.412	0.472	0.439	0.581
	LPIPS \downarrow	0.819	0.798	0.942	0.834	0.810	0.798	0.429
	CLIP-F \uparrow	93.53	93.80	93.62	95.52	94.10	95.90	94.97
	RotErr \downarrow	173.0	172.5	156.0	178.1	160.9	155.8	140.27
	TransErr \downarrow	0.035	0.029	0.049	0.022	0.023	0.016	0.022
	MatchPx \uparrow	0.004	0.009	0.001	0.006	0.004	0.008	0.008
	TempFlick \uparrow	0.931	0.948	0.971	0.952	0.959	0.958	0.955
	SubjCons \uparrow	0.806	0.753	0.710	0.789	0.807	0.869	0.829
	BGCons \uparrow	0.908	0.889	0.848	0.887	0.871	0.934	0.909
	ImagQual \uparrow	0.565	0.519	0.357	0.579	0.565	0.560	0.496
	AesQual \uparrow	0.953	0.784	0.453	0.978	0.884	0.986	0.445
MotSmooth \uparrow	0.384	0.691	0.916	0.619	0.624	0.659	0.775	
Objectron	PSNR \uparrow	10.43	9.19	14.59	11.50	11.62	9.51	15.14
	SSIM \uparrow	0.675	0.649	0.783	0.698	0.712	0.656	0.714
	LPIPS \downarrow	0.765	0.741	0.774	0.750	0.738	0.731	0.377
	CLIP-F \uparrow	94.14	94.19	93.62	95.53	94.92	95.06	94.36
	RotErr \downarrow	313.4	285.8	261.5	300.0	300.3	311.0	11.76
	TransErr \downarrow	0.076	0.087	0.103	0.046	0.058	0.028	0.018
	MatchPx \uparrow	0.001	0.004	0.000	0.001	0.001	0.002	0.003
	TempFlick \uparrow	0.949	0.968	0.928	0.964	0.965	0.962	0.966
	SubjCons \uparrow	0.801	0.770	0.651	0.787	0.804	0.839	0.759
	BGCons \uparrow	0.916	0.913	0.863	0.900	0.888	0.828	0.908
	ImagQual \uparrow	0.502	0.462	0.276	0.467	0.471	0.523	0.498
	AesQual \uparrow	0.456	0.228	0.111	0.484	0.300	0.469	0.343
MotSmooth \uparrow	0.532	0.854	0.976	0.752	0.797	0.663	0.784	
360°	PSNR \uparrow	4.71	4.31	3.39	4.62	5.25	5.40	11.26
	SSIM \uparrow	0.228	0.208	0.239	0.182	0.332	0.278	0.582
	LPIPS \downarrow	0.894	0.878	0.964	0.927	0.846	0.850	0.421
	CLIP-F \uparrow	92.66	94.31	93.95	94.13	93.32	94.92	93.74
	RotErr \downarrow	178.9	249.2	169.9	250.4	221.8	158.9	133.31
	TransErr \downarrow	0.038	0.061	0.071	0.041	0.030	0.030	0.050
	MatchPx \uparrow	0.005	0.007	0.001	0.005	0.005	0.009	0.007
	TempFlick \uparrow	0.896	0.923	0.956	0.916	0.930	0.912	0.924
	SubjCons \uparrow	0.801	0.763	0.724	0.762	0.768	0.826	0.748
	BGCons \uparrow	0.894	0.913	0.885	0.881	0.877	0.921	0.895
	ImagQual \uparrow	0.504	0.476	0.364	0.654	0.501	0.584	0.490
	AesQual \uparrow	0.999	0.841	0.741	0.908	0.758	0.996	0.403
MotSmooth \uparrow	0.144	0.445	0.641	0.162	0.264	0.312	0.496	
Omni-Object3D	PSNR \uparrow	5.70	4.75	4.49	5.43	5.90	7.07	9.36
	SSIM \uparrow	0.511	0.412	0.440	0.475	0.511	0.601	0.482
	LPIPS \downarrow	0.801	0.794	0.839	0.775	0.779	0.656	0.537
	CLIP-F \uparrow	94.51	95.05	93.95	94.87	95.29	95.06	94.78
	RotErr \downarrow	169.6	171.5	160.3	155.6	148.9	152.2	141.08
	TransErr \downarrow	0.109	0.150	0.113	0.141	0.091	0.052	0.013
	MatchPx \uparrow	0.002	0.004	0.000	0.002	0.002	0.008	0.004
	TempFlick \uparrow	0.953	0.972	0.981	0.967	0.975	0.962	0.971
	SubjCons \uparrow	0.810	0.768	0.741	0.707	0.830	0.840	0.793
	BGCons \uparrow	0.908	0.908	0.882	0.877	0.908	0.919	0.909
	ImagQual \uparrow	0.536	0.489	0.369	0.403	0.522	0.624	0.530
	AesQual \uparrow	0.932	0.846	0.609	0.823	0.860	0.930	0.450
MotSmooth \uparrow	0.549	0.857	0.896	0.576	0.791	0.677	0.881	
SynView-X	PSNR \uparrow	11.19	12.50	13.18	12.61	11.93	10.00	12.14
	SSIM \uparrow	0.470	0.417	0.537	0.555	0.538	0.428	0.586
	LPIPS \downarrow	0.676	0.624	0.734	0.666	0.665	0.644	0.456
	CLIP-F \uparrow	93.25	94.63	91.95	95.85	93.66	94.57	93.85
	RotErr \downarrow	54.37	41.51	69.73	66.64	50.66	58.50	29.63
	TransErr \downarrow	0.086	0.137	0.173	0.165	0.113	0.107	0.017
	MatchPx \uparrow	0.003	0.007	0.000	0.002	0.003	0.009	0.008
	TempFlick \uparrow	0.951	0.972	0.979	0.974	0.974	0.953	0.964
	SubjCons \uparrow	0.773	0.797	0.648	0.736	0.788	0.803	0.781
	BGCons \uparrow	0.901	0.920	0.875	0.901	0.884	0.915	0.899
	ImagQual \uparrow	0.421	0.440	0.245	0.346	0.385	0.547	0.421
	AesQual \uparrow	0.723	0.735	0.083	0.773	0.635	0.883	0.392
MotSmooth \uparrow	0.463	0.849	0.883	0.721	0.761	0.610	0.789	

Table 5: **Single-view** VBench video-quality metrics across 5 datasets (CO3D, Objectron, 360°, OmniObject3D, SynView-X). Refer to Section D for discussion on perceptual measures. Note that WarpHammer is the most accurate model in providing views that follow the camera trajectory (OrbErr).

Method	Consistency			Quality	Motion	Camera Pose	
	TempFlick↑	SubjCons↑	BGCons↑	ImagQual↑	MotSmooth↑	OrbErr↓	
Warp-based	TrajCr.	0.936	0.798	0.905	0.506	0.414	0.3022
	GEN3C	0.957	0.770	0.909	0.477	0.739	0.3058
	EX-4D	0.955	0.756	0.889	0.490	0.566	0.3192
	CogNVS	0.961	0.799	0.886	0.489	0.647	0.3063
	WF	0.965	0.779	0.888	0.484	0.577	0.3067
Camera-cond.	ReCamM.	0.963	0.695	0.871	0.322	0.862	0.3460
	SEVA	0.949	0.835	0.903	0.568	0.584	0.2855
	WarpHammer-TC	0.931	0.786	0.891	0.569	0.464	0.2288
WarpHammer-GEN3C	0.956	0.782	0.904	0.487	0.745	0.2045	

Table 6: **Auxiliary-view** VBench video-quality metrics across 5 datasets (CO3D, Objectron, 360°, OmniObject3D, SynView-X). Gray methods use GT camera poses and in-scene second views and are shown for reference only.

Method	Consistency			Quality	Motion	
	TempFlick↑	SubjCons↑	BGCons↑	ImagQual↑	MotSmooth↑	
w/ GT	GEN3C-MV	0.951	0.755	0.894	0.433	0.642
	SEVA-MV	0.954	0.812	0.904	0.576	0.501
w/o GT	GEN3C-MV	0.955	0.769	0.899	0.426	0.684
	SEVA-MV	0.938	0.769	0.886	0.581	0.442
	WarpHammer-GEN3C	0.966	0.785	0.905	0.471	0.835